MATERIALS SCIENCE

Ultrathin water-stable metal-organic framework membranes for ion separation

Meipeng Jian[1], Ruosang Qiu[1], Yun Xia[1], Jun Lu[1], Yu Chen[2], Qinfen Gu[3]*, Ruiping Liu[4,5], Chengzhi Hu[4], Jiuhui Qu[4,5], Huanting Wang[1], Xiwang Zhang[1]*

Owing to the rich porosity and uniform pore size, metal-organic frameworks (MOFs) offer substantial advantages over other materials for the precise and fast membrane separation. However, achieving ultrathin water-stable MOF membranes remains a great challenge. Here, we first report the successful exfoliation of two-dimensional (2D) monolayer aluminum tetra-(4-carboxyphenyl) porphyrin framework (termed Al-MOF) nanosheets. Ultrathin water-stable Al-MOF membranes are assembled by using the exfoliated nanosheets as building blocks. While achieving a water flux of up to 2.2 mol m^{-2} $hour^{-1}$ bar^{-1}, the obtained 2D Al-MOF laminar membranes exhibit rejection rates of nearly 100% on investigated inorganic ions. The simulation results confirm that intrinsic nanopores of the Al-MOF nanosheets domain the ion/water separation, and the vertically aligned aperture channels are the main transport pathways for water molecules.

INTRODUCTION

Ion separation with energy-efficient and environment-friendly membranes is essential in water environmental fields, e.g., wastewater recycling and seawater and brackish water desalination (*1*). Polymers are, by far, the most widespread membrane materials, largely owing to their easy processability and low cost (*2*). However, traditional polymeric membranes for ion separation from water are usually with a dense-selective layer, leading to the insurmountable permeability-selectivity trade-off, governed by the solution-diffusion model (*3*). In contrast, nanoporous membranes where nanopores act as the sieving role may overcome the limitation (*4*, *5*). In this regard, recent advances in nanoporous membranes, such as porous polymers, nanotube, zeolite, and aquaporin-based membranes, have witnessed substantial progress (*6*–*8*). The advancements collectively recognized the potential of nanoporous membranes in enhancing ion sieving capacity if the separation channels are properly designed. Nevertheless, most nanoporous membranes are usually thick at micrometer scale and are formed by discrete channels, hampering membrane permeability (*9*, *10*). Recently, two-dimensional (2D) materials, such as graphene oxide (GO), reduced GO, MoS_2, etc., have recently emerged as building blocks for membrane synthesis (*11*–*13*). These 2D nanosheets have constructed a new class of membranes with an ultrathin thickness, in which the interlayer space between adjacent nanosheets acts as selective nanochannels for ion sieving (*14*). Despite the thin architecture and special transport channels of these 2D laminar membranes, there are still deficiencies in separation performance, such as high transport tortuosity and insecure/improper interlayer distance (*15*, *16*).

Metal-organic frameworks (MOFs) are a scientifically compelling and evolving class of highly porous materials (*17*). Thus, MOFs are expected to be one of the most promising materials for separation membranes (*18*, *19*). In particular, the use of 2D MOF nanosheet-based membranes for gas separation holds the promise of making a breakthrough in achieving a simultaneous increase of both permeability and selectivity (*20*). However, it remains a daunting challenge to fabricate ultrathin MOF membranes (less than 100 nm) for water-related processing, since most reported MOF membranes are typically thick because of 3D crystal constitution and suffer from insufficient hydrolytic stability (*21*, *22*).

Here, we report the preparation of water-stable monolayer aluminum tetra-(4-carboxyphenyl)porphyrin framework (termed Al-MOF) nanosheets and demonstrate their excellence as building materials for membranes in ion separation from water. Exfoliated Al-MOF nanosheets exhibit a long-term structural robustness in aqueous environment and can form a laminar membrane via a facile vacuum filtration on porous substrates. The resulting 2D Al-MOF laminar membrane exhibits an extremely low permeability to tested ions (~3.3×10^{-6} mol m^{-2} $hour^{-1}$ bar^{-1}) but achieves water fluxes of up to 2.2 mol m^{-2} $hour^{-1}$ bar^{-1}. Overall, the 2D MOF membranes outperform the most reported 2D laminar membranes on the water/ion selectivity. In addition, the interlayer distance in the Al-MOF laminar membrane is self-locked via parallel π-π interactions, leading to a steady performance for more than 750 hours.

RESULTS AND DISCUSSION

Bulk-type Al-MOF crystals were obtained through a modified solvent-thermal method (*23*). The corresponding scanning electron microscopy (SEM) and atomic force microscopy (AFM) images (Fig. 1A and fig. S1, A and B) show a layered crystalline structure. Considering the weak interlayer bonding in the [0k0] direction of the bulk-type Al-MOF crystals, a facile sonication approach was used to successfully exfoliate them into 2D nanosheets (Method section and fig. S1C). Impressively, the convenient exfoliation route can reach a high nanosheet yield of approximately 90% (fig. S1D). The 2D ultrathin morphology of exfoliated Al-MOF nanosheets is revealed by transmission electron microscopy (TEM) images (Fig. 1B and fig. S2A). More than 80% of the Al-MOF nanosheets have a lateral size between 200 nm and 2 μm (fig. S2B). After the exfoliation, the Al-MOF

[1]Department of Chemical Engineering, Monash University, Clayton, Victoria 3800, Australia. [2]Monash Centre for Electron Microscopy, Monash University, Clayton, Victoria 3800, Australia. [3]Australian Synchrotron (ANSTO), Clayton, Victoria, 3168, Australia. [4]State Key Laboratory of Environmental Aquatic Chemistry, Research Center for Eco-Environmental Sciences, Chinese Academy of Sciences, Beijing 100085, China. [5]Center for Water and Ecology, State Key Joint Laboratory of Environment Simulation and Pollution Control, School of Environment, Tsinghua University, Beijing 100084, China. *Corresponding author. Email: xiwang.zhang@monash.edu (X.Z.); qinfeng@ansto.gov.au (Q.G.)

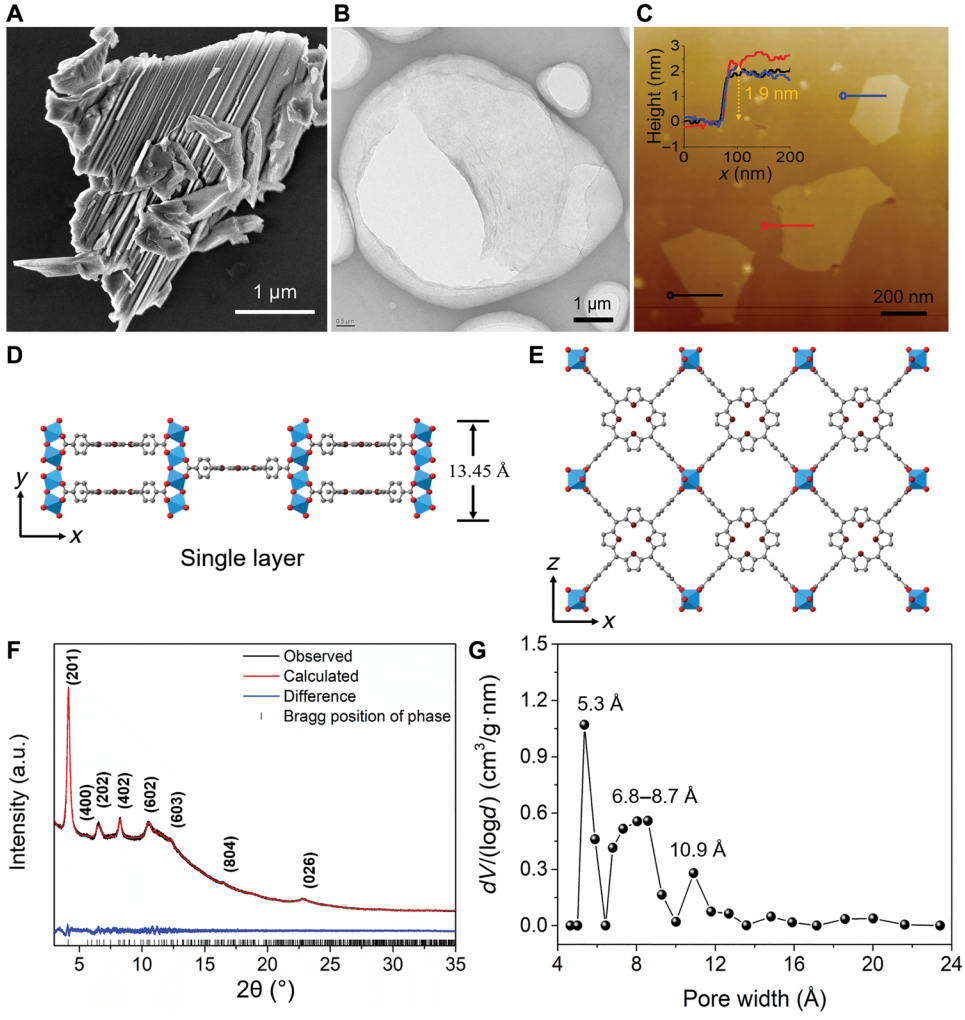

Fig. 1. Synthesis and structure of Al-MOF nanosheets. (**A**) SEM image of the representative Al-MOF bulk crystals. (**B**) TEM image of exfoliated Al-MOF nanosheets. (**C**) AFM topographical image of Al-MOF nanosheets on a silicon wafer. Inset is the corresponding height profile. (**D**) Single monolayer Al-MOF nanosheet viewed from the [001] direction. (**E**) Crystal structure of Al-MOF viewed down the [010] direction. The Al coordination polyhedra are depicted in blue, whereas nitrogen, oxygen, and carbon atoms are shown in purple, red, and gray, respectively. H atoms are omitted for clarity. (**F**) Rietveld refinement of the synchrotron XRD data of Al-MOF nanosheets. a.u., arbitrary units. (**G**) Pore-size distribution of Al-MOF nanosheets from N_2 adsorption-desorption measurement.

nanosheet suspension shows an excellent dispersibility, and the colloidal solution can be reserved for more than 2 months (fig. S2C). The thickness of Al-MOF nanosheets was measured by AFM to be around 1.9 nm (Fig. 1C), which is close to the theoretical height (~1.35 nm) of a monolayer Al-MOF nanosheet (Fig. 1D).

The crystallinity of Al-MOF nanosheets was examined by synchrotron x-ray powder diffraction (XRD). The crystal structures of Al-MOF crystals viewed down the [001] direction and the monolayer Al-MOF nanosheet viewed from the [010] direction are illustrated in Fig. 1 (D and E, respectively). The observed XRD pattern of exfoliated Al-MOF nanosheets fit well with the calculated patterns of monolayer Al-MOF nanosheets (Fig. 1F), confirming their inherent structural features of Al-MOF crystal. In addition, a selected-area electron diffraction pattern gives individual diffraction spots, demonstrating the single-crystal nature of the exfoliated Al-MOF nanosheets (fig. S3). Compared with Al-MOF bulks, XRD peaks of Al-MOF nanosheets are weak, and a few peaks even disappear (fig. S4), largely owing to the loss of diffraction signals in the out-of-plane direction and the nonplanar shape of the nanosheets (*24*). X-ray photoelectron spectroscopy (XPS), energy-dispersive spectroscopy (EDS), ultraviolet-visible spectra (UV-Vis), attenuated total reflectance Fourier transform infrared spectroscopy (ATR-FTIR), and thermogravimetric analysis (TGA) characterizations in figs. S5 to S9 further reveal that the exfoliated nanosheets preserve the structural integrity.

Exfoliated Al-MOF nanosheets also feature a microporous structure (type I isotherm) and give a specific surface area of 602 $m^2 g^{-1}$ (fig. S10A). Meanwhile, it displays authentic angstrom-size pores from experimental isotherm analyses in Fig. 1G. However, the pore distribution plot of Al-MOF nanosheets shows a slight difference from that of its bulk counterpart, which could be caused by the exfoliation effect and inevitable restacking of dried nanosheets along the [0k0] direction (fig. S10B). To assess the water stability, Al-MOF nanosheets were soaked in water for a month. The water-treated Al-MOF nanosheets exhibited identical XRD patterns to their initial status (fig. S11). Furthermore, the N_2 adsorption-desorption

isotherm and pore distribution of the Al-MOF nanosheets, after being immerged in water, were both similar to those of the pristine sample (fig. S12). Likewise, porphyrin ligand and Al^{3+} were not present in the filtrate after 1-month water stability test (fig. S13). These results confirm the unchanged crystallinity of Al-MOF nanosheets after prolonged immersion in water. In another aspect, Al-MOF nanosheets kept their characteristic diffraction peaks after being exchanged with NaCl (fig. S14A), which indicates that Al-MOF nanosheets could withstand exposure to inorganic ions, having a desired chemical endurance. In situ high-temperature synchrotron XRD characterization was also conducted on Al-MOF nanosheets from 50° to 190°C, and no obvious variations were observed on the phase transformations and crystalline lattices with the increase in temperature, which elucidates the pore rigidity in Al-MOF nanosheets (fig. S14, B to D).

A 2D Al-MOF laminar membrane (Fig. 2A) was assembled by vacuum filtration of a diluted Al-MOF nanosheet suspension (fig. S15) using anodic aluminum oxide (AAO) support with a pore size of 100 nm. In an apparent contrast to bare AAO support (Fig. 2B), a top-view SEM image of a ~10-nm-thick membrane shows a uniform coverage of Al-MOF nanosheets on the surface of AAO support, and no visible defects were observed (Fig. 2C). The continuous and flat Al-MOF laminar membrane was visualized by AFM and cross-sectional SEM characterizations (Fig. 2D and fig. S16). In addition, the membrane exhibits a hydrophilic character, demonstrated by a water contact angle of 44° (fig. S17). By controlling the loading of Al-MOF nanosheets, the thickness of the membranes can be precisely tuned from a few nanometers to micrometers (Fig. 2E and figs. S18 and S19). Notably, a typical homogeneous laminar structure is seen when the membrane thickness reaches 500 nm (Fig. 2E).

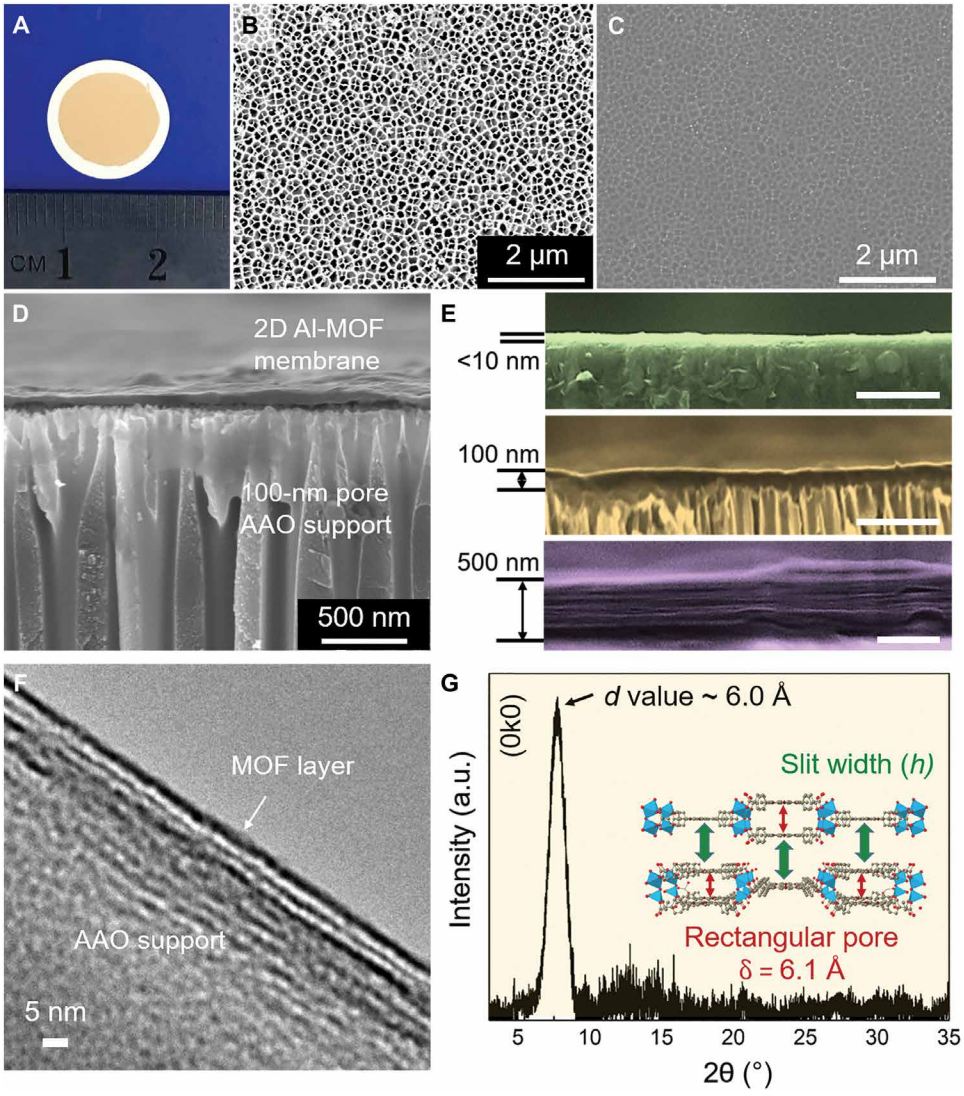

Fig. 2. Characterizations of Al-MOF membranes. (**A**) Digital photo of an as-prepared 100-nm-thick Al-MOF laminar membrane on AAO substrate. (**B**) SEM image of a bare AAO substrate. (**C**) SEM image of a sub–10-nm-thick Al-MOF laminar membrane on AAO substrate. The visibility of substrate background elucidates the ultrathin coverage. (**D**) Cross-sectional overview of a 100-nm-thick Al-MOF laminar membrane on AAO substrate. (**E**) Magnified cross-sectional views of 2D Al-MOF membranes with different thicknesses. Membranes less than 100 nm (green and gold) show a compact stacking, whereas the membrane at a thickness of 500 nm (purple) apparently shows typical laminar structure. Scale bars, 500 nm. (**F**) Cross-sectional TEM image of the 2D Al-MOF laminar membrane. (**G**) GIXRD pattern of the Al-MOF laminar membrane. The pattern was acquired from a thick membrane (~20 μm) due to the detection limit. The sharp (0k0) phase peak at $2\theta = 7.6°$ indicates an average value of 6.0 Å.

The laminar structure was also revealed by a cross-sectional TEM characterization (Fig. 2F). Furthermore, the synchrotron grazing incidence x-ray diffraction (GIXRD) analysis observed a prominent (0k0) peak at 2θ = 7.6°, showing the *d* value of ~6.0 Å. This manifests that the slit width (*h*) is close to the size of the rectangular pore in one layer (δ = 6.1 Å; Fig. 2G and inset).

The water permeation across the Al-MOF laminar membrane was first examined by measuring the weight loss of a container covered by a 100-nm-thick Al-MOF membrane (fig. S20). Figure 3A shows that the water evaporation rate of the sealed container is close to that of the open aperture (in the absence of the Al-MOF membrane). This demonstrates the unimpeded water vapor flow through the Al-MOF membrane. Afterward, we further investigated the permeation of the Al-MOF membrane for liquid water in a diffusion cell using deionized water and 0.5 M $CoCl_2$ as feed and draw solutions, respectively (fig. S21). The volume of the draw solution gradually increased with time, owing to water transport from the feed side driven by the osmotic pressure difference (Fig. 3B). The two experiments collectively show that the Al-MOF laminar membrane is permeable to water molecules. In the diffusion test, it is worth noting that the water permeance is dependent on the salt in the draw solutions. High water permeance was achieved by $AlCl_3$ and $CoCl_2$ solutions, whereas relatively low water permeance was achieved for NaCl, KCl, $MgCl_2$, and $CaCl_2$ solutions (Fig. 3C). This anomalous result might be caused by the difference in the affinity of these cations onto Al-MOF sheets, which was verified by an adsorption experiment (fig. S22). Further XPS characterization shows that aluminum hydroxyl groups from Al-MOF nanosheets play a vital role in adsorbing these ions (fig. S23). Considering that the adsorbed ions suppress water transport to some extent, surface modification to inhibit adsorption of ions could be a strategy in future studies to improve the water permeance of the Al-MOF membranes.

The permeation rates of these ions in the Al-MOF laminar membrane were also evaluated in the diffusion cell, using 0.5 M NaCl, KCl, $MgCl_2$, $CaCl_2$, $AlCl_3$, and $CoCl_2$, respectively. They are all ultralow, less than 3.3×10^{-6} mol m^{-2} $hour^{-1}$ bar^{-1} (Fig. 3C), which is generally considered impermeable (nearly 100% rejection) (*11*). Compared with other reported 2D laminar membranes, the Al-MOF membrane has a lower ion permeance (table S1). After the diffusion testing using NaCl, the surface and underneath layers of the used membrane were characterized by XPS. Except for the membrane surface, NaCl was hardly detected inside the membrane (fig. S24). This further verifies the hindrance of Al-MOF pores on the hydrated salts. In addition, anion species have no apparent impact on salt permeation (fig. S25). Because of the affinity of some salts (NaCl, KCl, $MgCl_2$, and $CaCl_2$) on Al-MOF active sites, the water permeance

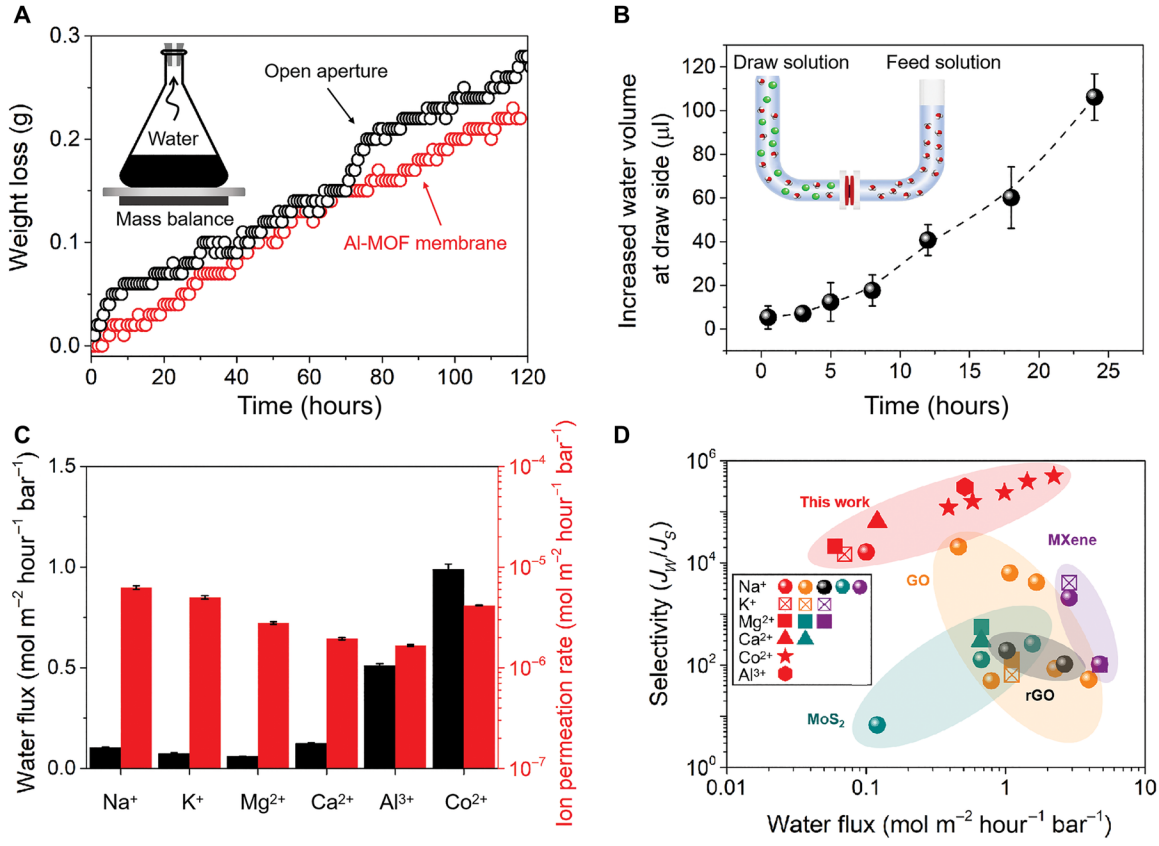

Fig. 3. Performances of Al-MOF membranes. (**A**) Water evaporation through the Al-MOF membrane. The figure depicts the weight loss of water from a container sealed with a 100-nm-thick Al-MOF membrane. Inset is a schematic setup for the water evaporation process. (**B**) Liquid volume change of the draw solution with time during the diffusion process. Feed side is DI water, whereas draw side is 0.5 M $CoCl_2$ aqueous solution. Inset is a schematic U-shaped setup for the diffusion process. (**C**) Water flux through a 100-nm-thick Al-MOF membrane using different draw solutions (0.5 M) and the corresponding ion permeation rates. (**D**) Correlation between water flux and water/salt selectivity of Al-MOF membranes and other representative 2D laminar membranes on different supports. The detailed data are listed in table S1. Each set of symbols represents a different salt.

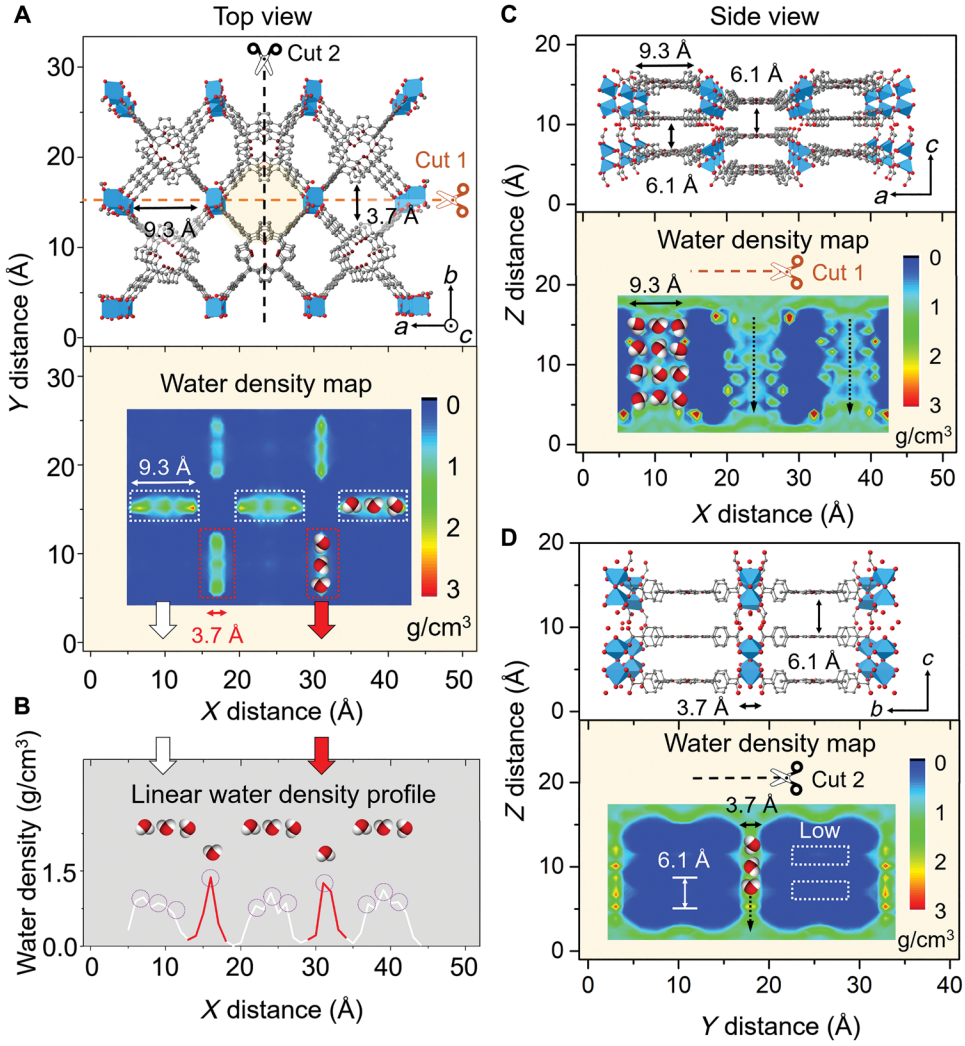

Fig. 4. Water transport behavior through Al-MOF membranes. (**A**) Crystalline illustration of Al-MOF membrane constructed with two-layer nanosheets under AB stacking sequence (viewed along the [010] direction). Dashed lines present two different incision positions for cross-sectional membrane geometries (marked with cut 1 and cut 2, respectively). Below figure is the corresponding water density map. The blue color corresponds to no water existence and the red corresponds to the maximum water density. (**B**) Linear water density profile collected from the upper water density map. White lines represent the water density in the three arranged pores (9.3 Å in the *X* axis × 3.7 Å in the *Y* axis), and red lines refer to that in the two arranged pores (3.7 Å in the *X* axis × 9.3 Å in the *Y* axis), as illustrated in white and red dashed rectangles, respectively. (**C**) Side view of the membrane at cut 1 section is viewed along the [001] direction, which gives the interlayer distance of 6.1 Å. Below figure is the corresponding water density map. (**D**) Side view of the membrane at cut 2 section is viewed along the [100] direction. White dashed rectangles stand for the low-water densities inside the interlayer space.

of Al-MOF laminar membranes is comparably low. Despite that, the water permeance of the Al-MOF membrane is still comparable to those of the state-of-the-art 2D laminar membranes when $AlCl_3$ and $CoCl_2$ are used as draw solutions (Fig. 3D). Notably, the water permeance of the Al-MOF membrane can be exponentially increased to 2.22 mol m^{-2} $hour^{-1}$ bar^{-1} by reducing the thickness down to 20 nm, while high salt rejection remains (fig. S26). Owing to the ultralow salt permeation, the water/ion selectivity of the Al-MOF laminar membrane reaches up to 5.00×10^5 (Fig. 3D and table S1), which outperforms most 2D laminar membranes on different substrates reported so far.

The long-term integrity of the Al-MOF membrane was examined by assessing the Na^+ permeation rate and water flux in a continuous testing. As shown in fig. S27, the steady plot of Na^+ concentration at the feed side and a constant water flux of the membrane over 30 days were observed, confirming the long-lasting stability. The superior stability of Al-MOF membranes should be attributed to the locking effect of adjacent nanosheets by means of parallel π-π interaction (*25*, *26*). Meanwhile, fig. S28 gives the unchanged reflection (0k0) peak at $2\theta = 7.6°$ of the Al-MOF membrane after 1-month continuous testing. Furthermore, the antiswelling ability of Al-MOF membranes were visually examined (fig. S29). In addition to the AAO substrate, Al-MOF laminar membranes with similar performance were also successfully synthesized on low-cost polymer substrates such as polycarbonate and polyethersulfone (fig. S30).

Molecular dynamics (MD) simulations were conducted to gain insights into salt rejection and water transport in the Al-MOF membrane. First, the kinetic behavior of water and ion transport

across the pore aperture of Al-MOF membranes was simulated. In accordance with the experimental results, all examined ions are effectively blocked by the Al-MOF nanopores, whereas water molecules are allowed to penetrate on the basis of size exclusion (table S2 and fig. S31). Although both AA and AB stacking regimes are theoretically possible when Al-MOF nanosheets are assembled into membranes, density functional theory (DFT) calculation reveals that AB stacking is more likely than AA stacking due to a lower DFT energy (fig. S32). The DFT calculation also shows that the interlayer space of the Al-MOF laminar membrane formed via AB stacking is 6.1 Å, which is consistent with the GIXRD characterization (Fig. 2G and fig. S32). Therefore, on the basis of AB stacking, an MD model for the Al-MOF laminar membrane was built, which consists of two-layer Al-MOF nanosheets (Fig. 4), to compute the probability distribution of water molecules inside the membrane.

The water density map (Fig. 4A) reveals that the water flow is highly localized to the intrinsic pores of Al-MOF nanosheets. Furthermore, the corresponding linear gradient profile (Fig. 4B) indicates that water molecules align side by side when flowing through these pores (as illustrated in the water density map) due to confined space. The side views of water transport channels of the AB stacked membrane are presented by using two incision positions (Fig. 4, C and D). Most of the water molecules are observed in the straight channels (the vertically aligned intrinsic pores of neighboring Al-MOF nanosheets), whereas a small amount of water is in the interlayer spaces, as indicated with white dashed rectangles (Fig. 4, C and D). This is in agreement with the water trajectory results, which show that most water molecules flow through the Al-MOF membrane via the vertically aligned aperture channels (straight flow), and only 17.08% of water molecules shift from one channel to another via the interlayer space (shift flow) when passing through the membrane (fig. S33). Similar water dynamic behavior was observed in AA stacking model (fig. S34), although the shift flow is much more likely to occur because of the relatively larger interlayer spaces (6.2 and 12.5 Å). Furthermore, the MD simulations on NaCl diffusion reveal that salt species cannot permeate through the slit channels between the nanosheets in both AB and AA stacked membranes (fig. S35).

CONCLUSION

Our findings demonstrated the fabrication of ultrathin nanoporous membranes assembled by 2D MOF nanosheets for ion separation from water. The obtained laminar membrane exhibited an excellent long-term stability in water, against the intractable swelling for 2D-based membranes. All the tested ions had ultralow permeation rates, which were attributed to the Al-MOF pore hindrance. Water transport mainly occurs in the vertically aligned aperture channels formed by the intrinsic pores of Al-MOF nanosheets. This membrane opens up the possibility to explore emerging nanoporous-based membranes and meets the critical need for increased selectivity for desalination membranes (*27*). However, we envisage that full understanding of the membrane requires further efforts in terms of aperture shape, channel charge, transport friction, pore density, etc.

MATERIALS AND METHODS

Materials

$Al(NO_3)_3{\cdot}9H_2O$, pyrazine, and *p*-xylene were all purchased from Sigma-Aldrich. Tetrakis(4-carboxyphenyl) porphyrin (H_2TCPP, 97%) was purchased from Tokyo Chemical Industry Co. Ltd. All salt powders, *N*,*N*-dimethylformamide (DMF), and ethanol were purchased from Merck. All the chemicals were of analytical grade and were used as received without further purification. Deionized water used in all experiments was from a Milli-Q system (Advantage A10, Merck Millipore, USA). AAO disc filters (100-nm pore, 13-mm diameter) were purchased from GE Healthcare Whatman. Polyethersulfone (PES; 30-nm pore, 13-mm diameter) and polycarbonate track etch (PCTE; 100-nm pore, 25-mm diameter) membrane filters were purchased from Steritech.

Methods

Synthesis of Al-MOF bulks

Bulk-type Al-MOF was prepared following a modified method in our previous study (*28*). First, 93.23 mg of $Al(NO_3)_3{\cdot}9H_2O$, 14 mg pyrazine, 150 ml of *N*,*N*-dimethylformamide (DMF), and 50 ml of ethanol were mixed in a 250-ml Schott Duran bottle and sonicated 30 min to dissolve completely at room temperature. This is the Al precursor solution for Al-MOF production. Second, 200 mg of tetrakis(4-carboxyphenyl)porphyrin (H_2TCPP) was dissolved in 200 ml of DMF with an assistance of 30-min sonication. This is the ligand solution for Al-MOF synthesis. Al-MOF bulks were synthesized in a typical procedure by pipetting 8 ml of Al precursor solution and 4 ml of the ligand solution in a 20-ml glass vial, respectively. The glass vial was then capped, and the mixture was stirred on an orbital vortex shaker (Labco) for 1 min. Afterward, the capped vials were heated to 120°C for 16 hours in an oil bath. Last, the resulting purple precipitate was collected by centrifugation and washed three times with 40 ml of absolute ethanol.

Sonication exfoliation of Al-MOF bulks to monolayer nanosheets

Likewise, Al-MOF bulks from four glass vials were obtained after the solvent-thermal reaction. The purple resultant was washed with absolute 40 ml of DMF twice and 40 ml of ethanol once, respectively. The final dispersion in ethanol was then bath-sonicated for 3 hours using a Unisonics FXP12M sonic bath (40 kHz, 100 W). To combat the considerable water heating caused by consecutive sonication, the bath water was renewed periodically every 30 min. After sonication, the suspension becomes highly dispersed. To remove the unexfoliated bulks, the dispersion was centrifuged (Sigma 2-16P) at 8500 rpm for 30 min. The retained supernatant was thus used for membrane assembling. The exfoliation yield rate was calculated through UV-Vis monitor, as shown in fig. S2 (D and E). To obtain dried samples of Al-MOF nanosheets and bulks for future characterizations, we used a freeze-drying process, which was performed in a freeze dryer (FreeZone 2.5 liters, Labconco Corporation, USA). For the sake of eliminating water interference, the as-synthesized Al-MOF nanosheets and bulks were dried by freezing their colloidal suspensions in *p*-xylene and removing the solvent via freeze-drying for 3 days. Al-MOF nanosheets after the water stability test were dried following the same processes as described above, except that water was used as the solvent.

Preparation of Al-MOF nanosheet aqueous suspension (1 mg/liter)

Original Al-MOF nanosheet dispersion in ethanol was calibrated at 2000 mg/liter by a UV-Vis spectrophotometer based on the predetermined standard curve (fig. S2, D and E). We then diluted the above dispersion to 1 mg/liter with deionized (DI) water for membrane preparation, as shown in fig. S14.

Membrane fabrication

Al-MOF membranes were fabricated by a vacuum filtration (Welch, 2511 WOB-L Pump) of the diluted Al-MOF nanosheet aqueous

suspension (1 mg/liter) on the prescribed porous substrates (see more information of these substrates in "Materials" section). The Al-MOF nanosheet loading (μg/mm^2) or membrane thickness (nm) was controlled by varying the volume of the Al-MOF suspension to be filtered. For consistency, the membranes described in this work were all 100 nm thick, unless specified otherwise. The resultant membranes were dried in an oven at 60°C overnight and then stored in a vacuum desiccator before testing.

Membrane sealing

Please refer to fig. S21 for detailed steps.

Characterization

X-ray powder diffraction. Because of the detection limit of laboratory x-ray sources, the structure and phase transformation of Al-MOF samples were determined by using synchrotron XRD. Al-MOF nanosheets and bulk samples were loaded in 0.5-mm ID Kapton capillaries, which were sealed at both ends with a Loctite adhesive. The patterns were collected at an energy of 18 keV ($\lambda = 0.812$ Å) and a MYTHEN-II capillary detector ($d = 250$ mm) on the high-resolution powder diffraction beamline at Australian Synchrotron (ANSTO). With regard to the membrane specimens, GIXRD is a powerful method to provide information of the interlayer distance d (nm). However, owing to the x-ray diffraction detection limit for thin membranes, we elaborately prepared a thick freestanding membrane (~ 20 μm) to harvest the signals. The thick freestanding Al-MOF membrane was first fabricated by vacuum filtration of Al-MOF nanosheets on a PCTE support and then slowly transferred in DMF solvent (membrane side face up). After approximately 5 min, PCTE substrate was completely dissolved in DMF, and the thick freestanding Al-MOF membrane would be floated on the surface of DMF. Afterward, a square transparent microscope glass slide (35 cm by 35 cm, 1-mm thickness, Thermo Fisher Scientific) was used to make the isolated membrane integral seated on the surface. In the end, the thick membrane on the slide was dried for 2 days in the oven at 80°C.

Field-emission scanning electron microscope. The morphology of the samples was detected via a field-emission scanning electron microscope (FESEM; FEI Magellan 400 XHR) equipped with EDS. For examining morphologies of Al-MOF nanosheets and bulks, one drop (1-cm-diameter pipette tip) of their ethanol suspensions (2 mg/liter) was deposited on a fresh 1 cm by 1 cm square of silicon wafer and then dried in air. Cross section of the supported membranes was prepared by breaking the membranes deposited on AAO substrates using a fine tweezer. All SEM specimens were coated with iridium (1.5 to 2.0 nm thick) to eliminate charging effect.

Transmission electron microscope. A FEI Tecnai G^2 T20 TWIN operated at 200 kV was used for TEM studies. All images were recorded using a charge-coupled device camera. Samples of Al-MOF nanosheets and bulks were prepared by adding one drop (1-cm-diameter pipette tip) of their ethanol dispersion (2 mg/liter) on holey carbon grids (230 mesh Cu, EMC) and were air-dried. Cross-sectional TEM examination for membrane specimens was carried out using a Leica UltraCut S ultramicrotome with a diamond knife. The sections were then mounted on holey carbon film copper grids (400 mesh Cu, Pelco), and the prepared samples were air-dried overnight for further microscope observations.

Atomic force microscopy. AFM images were collected using a Bruker Dimension Icon. Nanosheet and bulk specimens were prepared by placing a drop of their ethanol suspensions on a fresh 1 cm by 1 cm square of silicon wafer followed by air-drying. AFM cantilever tips from RTESPA (MPP-11120-10) were used. The analysis was performed in a tapping mode under air. The image analysis was performed with the software NanoScope Analysis version 1.5.

Thermogravimetric analysis. TGA was performed on a Perkin-Elmer STA 6000. Dried samples of nanosheets and bulks were both heated from 25° to 800°C at a rate of 10°C/min in air.

N_2 adsorption-desorption isotherms. N_2 adsorption-desorption isotherms of these samples were measured by a Micromeritics ASAP 2020 volumetric adsorption analyzer at liquid nitrogen temperature (77 K). Samples of nanosheets and bulks were both degassed at 150°C for 12 hours under vacuum before measurement.

Attenuated total reflectance Fourier transform infrared spectra. Functional groups of nanosheets and bulks were identified by a PerkinElmer ATR-FTIR spectrometer with a diamond crystal and resolution of 4 cm^{-1} by averaging the measurements over 16 scans. An average of 10 adjacent points from the diamond crystal detector was smoothly applied to the dried nanosheets and bulk samples.

Zeta potential measurement. Zetasizer (Malvern Nano ZS, UK) was used to determine the surface zeta potential of Al-MOF nanosheets. Each sample scan was repeated three times. Al-MOF nanosheet water suspension (5 mg/liter) at different pHs was prepared for the measurement.

X-ray photoelectron spectra. X-ray photoelectron spectra were determined by using an AXIS Ultra spectrometer (Kratos Analytical, Manchester, UK) with an Al K anode (1486.6-eV photon energy, 0.05-eV photon energy resolution, 300 W).

Ultraviolet-visible spectra. UV-Vis spectra were recorded on a UV spectrophotometer (Shimadzu UV-2401PC). Both Al-MOF nanosheets and bulk suspensions were prepared at 5 mg/liter for the measurement.

Inductively coupled plasma optical emission spectroscopy. Inductively coupled plasma optical emission spectroscopy (ICP-OES) from PerkinElmer (Optima 7000 DV) was used to quantify the concentration of ions in the ion separation experiment.

Contact angle. The static contact angle of the Al-MOF membrane was measured by placing a droplet of water (2 μl) on the membrane using a capillary with a diameter of 0.7 mm (OCA 15EC, DataPhysics, Germany). The equipped digital camera was used to monitor the shape of the droplet immediately after the droplet deposition. The average value of the contact angle was determined from the measurements of the contact angles at seven different locations on membranes.

Ion separation tests of the Al-MOF membranes

The sealing steps of Al-MOF membranes into diffusion cells refer to fig. S20A. Considering the potential deformity of the thin Al-MOF membranes caused by an external pressure, the separation performance was evaluated using a self-made diffusion cell as shown in fig. S20B, in which the permeation process was driven by an osmotic pressure. Al-MOF membranes facing draw solution were tightly fixed in the middle by clamps. Different concentrations (0.02, 0.05, 0.10, 0.20, 0.50, and 1.00 M) of salt solutions (NaCl, $NaNO_3$, Na_2SO_4, KCl, $MgCl_2$, $CaCl_2$, $CoCl_2$, and $AlCl_3$, respectively) were used as the draw solutions. Deionized water was used as the feed solution. Magnetic stirring was applied in both draw and feed sides to alleviate the external concentration polarization effect. The mass change of the draw solution was measured by monitoring the height increase of liquid level at the draw solution side (the draw-side compartment was reformed with 1.5-mm inner diameter at the top; fig. S20B). The salt leakage into the feed solution was monitored by a conductivity

meter (labCHEM-CP) and ICP-OES. The system temperature was maintained at 25° ± 0.5°C throughout the experiment. The water flux (J_w; mol m^{-2} h^{-1}) and salt ion permeation rate (J_s; mol m^{-2} $hour^{-1}$) of Al-MOF membranes were calculated as follows (*29*)

$$J_w = \frac{\Delta V}{A \cdot \Delta t}$$
$$J_s = \frac{(C_t \cdot V_t) - (C_0 \cdot V_0)}{A \cdot \Delta t \cdot M_w}$$

where ΔV is the volume change (μl = 5.6×10^{-5} mol) of the draw solution over a running time interval Δt (hours) in each experiment. A is the effective area of the Al-MOF membrane (7 mm^2). C_0 and V_0 denote the initial salt concentration (M) and feed solution volume (ml), while C_t and V_t are their responding values at a given time t. M_w is the molecular weight of salts (g/mol).

The water/salt selectivity $\frac{J_w}{J_s}$ is defined as the ratio of the water flux to salt ion permeation rate (*30*–*32*).

Water evaporation test of the Al-MOF membranes

For evaporation test, 30 ml of water was filled in a 150-ml flask in each run. A rubber with 8-mm straight pore was plugged in the top neck, and waterproof glue surrounds the edge to avoid any leakage. Sealed Al-MOF membranes (7 mm^2) were strongly glued on the top rubber of the flask by the carbon tabs (ProSciTech). The entire apparatus was under a dark environment and running at a stable temperature of 25° ± 0.5°C. The weight loss was constantly monitored using a digital computer-controlled balance (AND FX-3000i).

Salts adsorption capacity on Al-MOF nanosheets

Adsorption isotherm experiments were conducted in 20-ml plastic vials containing salt solution (10 ml) and Al-MOF nanosheet powder (10 mg). The initial concentrations of these salts were 0.02, 0.05, 0.10, 0.20, 0.50, and 1.0 M, respectively. The vials were shaken at 200 rpm for 24 hours at 25°C. Before the adsorption experiments, the mixture suspensions were sonicated for 10 min to alleviate aggregation. Solutions after adsorption were filtered with syringe prefilters (PTFE Millipore; pore size, 0.2 μm). The concentration change of each salt solution before and after adsorption was determined by measuring the conductivity. The adsorption capacity q (mmol/g) was calculated as follows (*33*)

$$q = \frac{\Delta C \cdot V}{m}$$

where ΔC (M) is the concentration difference of salt solution before and after salt adsorption, V (ml) is the volume of salt solution, and m (mg) is the adsorbent weight.

DFT calculations

DFT calculations were performed using the Vienna Ab initio Simulation Package 5.4.4 code on Australian Synchrotron Compute Infrastructure. The generalized gradient approximation with a Perdew-Burke-Ernzerhof exchange correlation function was used. The interactions between the ionic cores and the valence electrons were treated by ultrasoft pseudopotentials with atomic pseudopotentials corresponding to Na $3s^1$, K $3s^23p^64s^1$, Mg $3s^2$, Ca $3s^23p^64s^2$, Co $3d^84s^1$, and Al $3s^23p^1$. The zero-damping DFT-D3 dispersion correction method of Grimme was used to account for the importance of van der Waals interactions of the adsorption of ions and interlayers of Al-MOF in the system. In all calculations, the cutoff energy of the plane wave was set at 400 eV, and Monkhorst Pack k-point was used to ensure the total energy value convergence within 1 meV per atom.

DFT geometry optimization was conducted to reveal the most stable stacking configuration of Al-MOF nanosheet-assembled membranes. Figure S32 shows the typical stacking configurations of the stacked membrane models from two-layer Al-MOF nanosheets. From our calculations, it shows that the binding energy of two-layer Al-MOF nanosheets in AB stacking are the lowest, revealing the most stable structure.

MD simulations

All-atom molecular structures of Al-MOF membranes were built on the basis of the results of DFT simulations and charged via the Gasteiger method (*34*). Solvating the fixed membranes according to the requirements of (i) soaking and (ii) diffusion processes is further described below. One free-vibrating impermeable sheet was placed at each end of the reservoir, which was far away from the simulation box boundary, to maintain the system equilibrium. Later on, we extended the system with periodic boundary condition in all directions. The simulations were undertaken by Not Another Molecular Dynamics (NAMD) program (Git-2018-09-13 Linux-x86_64-multicore) with a 2-fs time step under 300 K that was performed in the NVT ensemble. Nonbonded interaction was calculated with CHARMM General Force Field and Multivalent Ion Force Field (*35*), which were applied with Lorentz-Berthelot mixing rules. Its cutoff radius was used with 12 Å. Particle mesh Ewald was used for long-range electrostatic interaction, and SHAKE Algorithm was applied on TIP3P water molecules.

1) Soaking process: Solvating fixed two-layer AA or AB stacked Al-MOF nanosheets (the corresponding interlayer distance is based on DFT results) with water molecules; averaging out the number of water molecules inside membranes over 4 ns for membrane water distribution and transport trajectory.

2) Diffusion process: Solvating fixed one-layer Al-MOF nanosheets with water molecules and ionized one side with 0.5 M $AlCl_3$, $CoCl_2$, $CaCl_2$, $MgCl_2$, NaCl, and KCl, respectively; collecting the total number of water molecules at the ionized side over 30 ns for calculating transmembrane water flux.

3) NaCl rejection performance by the slit channel: Two-layer Al-MOF nanosheets were built for illustration. The middle part of the first Al-MOF nanosheet crystalline was subtracted, while the second Al-MOF nanosheet crystalline was a short nanosheet to cover the defect and form the required slit channel with the first layer; solvating the membrane with water molecules and ionized one side with 0.5 M NaCl. The corresponding NaCl concentration was averaged from a 2-ns filtration process.

SUPPLEMENTARY MATERIALS

Supplementary material for this article is available at http://advances.sciencemag.org/cgi/content/full/6/23/eaay3998/DC1

REFERENCES AND NOTES

1. M. R. Chowdhury, J. Steffes, B. D. Huey, J. R. McCutcheon, 3D printed polyamide membranes for desalination. *Science* **361**, 682–686 (2018).
2. W. J. Koros, C. Zhang, Materials for next-generation molecularly selective synthetic membranes. *Nat. Mater.* **16**, 289–297 (2017).
3. J. R. Werber, C. O. Osuji, M. Elimelech, Materials for next-generation desalination and water purification membranes. *Nat. Rev. Mater.* **1**, 16018 (2016).
4. D. L. Gin, R. D. Noble, Designing the next generation of chemical separation membranes. *Science* **332**, 674–676 (2011).
5. H. B. Park, J. Kamcev, L. M. Robeson, M. Elimelech, B. D. Freeman, Maximizing the right stuff: The trade-off between membrane permeability and selectivity. *Science* **356**, eaab0530 (2017).

6. P. Wang, M. Wang, F. Liu, S. Y. Ding, X. Wang, G. Du, J. Liu, P. Apel, P. Kluth, C. Trautmann, Y. Wang, Ultrafast ion sieving using nanoporous polymeric membranes. *Nat. Commun.* **9**, 569 (2018).
7. M. Tsapatsis, Toward high-throughput zeolite membranes. *Science* **334**, 767–768 (2011).
8. R. H. Tunuguntla, R. Y. Henley, Y. C. Yao, T. A. Pham, M. Wanunu, A. Noy, Enhanced water permeability and tunable ion selectivity in subnanometer carbon nanotube porins. *Science* **357**, 792–796 (2017).
9. B. J. Hinds, N. Chopra, T. Rantell, R. Andrews, V. Gavalas, L. G. Bachas, Aligned multiwalled carbon nanotube membranes. *Science* **303**, 62–65 (2004).
10. I. Stassen, M. Styles, G. Grenci, H. Van Gorp, W. Vanderlinden, S. De Feyter, P. Falcaro, D. De Vos, P. Vereecken, R. Ameloot, Chemical vapour deposition of zeolitic imidazolate framework thin films. *Nat. Mater.* **15**, 304–310 (2016).
11. R. K. Joshi, P. Carbone, F. C. Wang, V. G. Kravets, Y. Su, I. V. Grigorieva, H. A. Wu, A. K. Geim, R. R. Nair, Precise and ultrafast molecular sieving through graphene oxide membranes. *Science* **343**, 752–754 (2014).
12. H. Liu, H. Wang, X. Zhang, Facile fabrication of freestanding ultrathin reduced graphene oxide membranes for water purification. *Adv. Mater.* **27**, 249–254 (2015).
13. Y. Kang, Y. Xia, H. Wang, X. Zhang, 2D laminar membranes for selective water and ion transport. *Adv. Funct. Mater.* **29**, 1902014 (2019).
14. Z. Zheng, R. Grünker, X. Feng, Synthetic two-dimensional materials: A new paradigm of membranes for ultimate separation. *Adv. Mater.* **28**, 6529–6545 (2016).
15. B. Mi, Materials science. Graphene oxide membranes for ionic and molecular sieving. *Science* **343**, 740–742 (2014).
16. J. Wang, P. Chen, B. Shi, W. Guo, M. Jaroniec, S.-Z. Qiao, A regularly channeled lamellar membrane for unparalleled water and organics permeation. *Angew. Chem. Int. Ed. Engl.* **57**, 6814–6818 (2018).
17. H. Furukawa, N. Ko, Y. B. Go, N. Aratani, S. B. Choi, E. Choi, A. O. Yazaydin, R. Q. Snurr, M. O'Keeffe, J. Kim, O. M. Yaghi, Ultrahigh porosity in metal-organic frameworks. *Science* **329**, 424–428 (2010).
18. S. Qiu, M. Xue, G. Zhu, Metal-organic framework membranes: From synthesis to separation application. *Chem. Soc. Rev.* **43**, 6116–6140 (2014).
19. X. Li, Y. Liu, J. Wang, J. Gascon, J. Li, B. Van der Bruggen, Metal–organic frameworks based membranes for liquid separation. *Chem. Soc. Rev.* **46**, 7124–7144 (2017).
20. Y. Peng, Y. Li, Y. Ban, H. Jin, W. Jiao, X. Liu, W. Yang, Membranes. Metal-organic framework nanosheets as building blocks for molecular sieving membranes. *Science* **346**, 1356–1359 (2014).
21. M. S. Denny Jr., J. C. Moreton, L. Benz, S. M. Cohen, Metal–organic frameworks for membrane-based separations. *Nat. Rev. Mater.* **1**, 16078 (2016).
22. A. J. Howarth, Y. Liu, P. Li, Z. Li, T. C. Wang, J. T. Hupp, O. K. Farha, Chemical, thermal and mechanical stabilities of metal–organic frameworks. *Nat. Rev. Mater.* **1**, 15018 (2016).
23. A. Fateeva, P. A. Chater, C. P. Ireland, A. A. Tahir, Y. Z. Khimyak, P. V. Wiper, J. R. Darwent, M. J. Rosseinsky, A water-stable porphyrin-based metal–organic framework active for visible-light photocatalysis. *Angew. Chem. Int. Ed.* **51**, 7440–7444 (2012).
24. Y. Jiang, L. Cao, X. Hu, Z. Ren, C. Zhang, C. Wang, Simulating powder X-ray diffraction patterns of two-dimensional materials. *Inorg. Chem.* **57**, 15123–15132 (2018).
25. S. Motoyama, R. Makiura, O. Sakata, H. Kitagawa, Highly crystalline nanofilm by layering of porphyrin metal–organic framework sheets. *J. Am. Chem. Soc.* **133**, 5640–5643 (2011).
26. R. Makiura, S. Motoyama, Y. Umemura, H. Yamanaka, O. Sakata, H. Kitagawa, Surface nano-architecture of a metal–organic framework. *Nat. Mater.* **9**, 565–571 (2010).
27. J. R. Werber, A. Deshmukh, M. Elimelech, The critical need for increased selectivity, not increased water permeability, for desalination membranes. *Environ. Sci. Technol. Lett.* **3**, 112–120 (2016).
28. M. P. Jian, H. Y. Liu, T. Williams, J. S. Ma, H. T. Wang, X. W. Zhang, Temperature-induced oriented growth of large area, few-layer 2D metal-organic framework nanosheets. *Chem. Commun.* **53**, 13161–13164 (2017).
29. M. Rastgar, A. Bozorg, A. Shakeri, Novel dimensionally controlled nanopore forming template in forward osmosis membranes. *Environ. Sci. Technol.* **52**, 2704–2716 (2018).
30. W. A. Phillip, J. S. Yong, M. Elimelech, Reverse draw solute permeation in forward osmosis: Modeling and experiments. *Environ. Sci. Technol.* **44**, 5170–5176 (2010).
31. Y. Wang, R. Ou, H. Wang, T. Xu, Graphene oxide modified graphitic carbon nitride as a modifier for thin film composite forward osmosis membrane. *J. Membr. Sci.* **475**, 281–289 (2015).
32. N.-N. Bui, J. R. McCutcheon, Nanoparticle-embedded nanofibers in highly permselective thin-film nanocomposite membranes for forward osmosis. *J. Membr. Sci.* **518**, 338–346 (2016).
33. J. Tóth, *Adsorption: Theory, Modeling, and Analysis* (Marcel Dekker Inc., 2002), vol. 107, 878 pp.
34. J. Gasteiger, M. Marsili, Iterative partial equalization of orbital electronegativity—A rapid access to atomic charges. *Tetrahedron* **36**, 3219–3228 (1980).
35. P. Li, L. F. Song, K. M. Merz Jr., Parameterization of highly charged metal ions using the 12-6-4 LJ-type nonbonded model in explicit water. *J. Phys. Chem. B* **119**, 883–895 (2014).
36. X. Zou, G. Zhu, I. J. Hewitt, F. Sun, S. Qiu, Synthesis of a metal-organic framework film by direct conversion technique for VOCs sensing. *Dalton Trans.* 3009–3013 (2009).
37. A. Fidalgo-Marijuan, G. Barandika, B. Bazán, M. K. Urtiaga, E. S. Larrea, M. Iglesias, L. Lezama, M. I. Arriortua, Heterogeneous catalytic properties of unprecedented μ-*O*-[FeTCPP]$_2$ dimers (H_2TCPP = *meso*-tetra(4-carboxyphenyl)porphyrin): An unusual superhyperfine EPR structure. *Dalton Trans.* **44**, 213–222 (2015).
38. H.-Y. Zeng, J.-Z. Du, S. Xu, M.-C. Liao, X.-J. Liu, H.-Z. Duan, C.-R. Chen, Influences of a glycerin co-solvent on the compatibility of MgAl hydrotalcites with a polypropylene matrix. *RSC Adv.* **5**, 64814–64820 (2015).
39. L. G. Joyner, E. P. Barrett, R. Skold, The determination of pore volume and area distributions in porous substances. II. Comparison between nitrogen isotherm and mercury porosimeter methods. *J. Am. Chem. Soc.* **73**, 3155–3158 (1951).
40. W. L. Xu, C. Fang, F. Zhou, Z. Song, Q. Liu, R. Qiao, M. Yu, Self-assembly: A facile way of forming ultrathin, high-performance graphene oxide membranes for water purification. *Nano Lett.* **17**, 2928–2933 (2017).
41. L. Chen, G. Shi, J. Shen, B. Peng, B. Zhang, Y. Wang, F. Bian, J. Wang, D. Li, Z. Qian, G. Xu, G. Liu, J. Zeng, L. Zhang, Y. Yang, G. Zhou, M. Wu, W. Jin, J. Li, H. Fang, Ion sieving in graphene oxide membranes via cationic control of interlayer spacing. *Nature* **550**, 380–383 (2017).
42. J. Abraham, K. S. Vasu, C. D. Williams, K. Gopinadhan, Y. Su, C. T. Cherian, J. Dix, E. Prestat, S. J. Haigh, I. V. Grigorieva, P. Carbone, A. K. Geim, R. R. Nair, Tunable sieving of ions using graphene oxide membranes. *Nat. Nanotechnol.* **12**, 546–550 (2017).
43. W. Hirunpinyopas, E. Prestat, S. D. Worrall, S. J. Haigh, R. A. W. Dryfe, M. A. Bissett, Desalination and nanofiltration through functionalized laminar MoS_2 membranes. *ACS Nano* **11**, 11082–11090 (2017).
44. M. Deng, K. Kwac, M. Li, Y. Jung, H. G. Park, Stability, molecular sieving, and ion diffusion selectivity of a lamellar membrane from two-dimensional molybdenum disulfide. *Nano Lett.* **17**, 2342–2348 (2017).
45. Z. Lu, Y. Wei, J. Deng, L. Ding, Z. K. Li, H. Wang, Self-crosslinked MXene ($Ti_3C_2T_x$) membranes with good antiswelling property for monovalent metal ion exclusion. *ACS Nano* **13**, 10535–10544 (2019).
46. R. A. Robinson, R. H. Stokes, *Electrolyte Solutions* (Dover Publications, ed. 2, 2002).

Acknowledgments: This work was performed in part at the Melbourne Centre for Nanofabrication (MCN) in the Victorian Node of the Australian National Fabrication Facility (ANFF). We thank the Australian Synchrotron for the use of the Powder Diffraction Beamline. We also acknowledge the use of facilities within the Monash Centre for Electron Microscopy (MCEM) and the Monash X-ray Platform (MXP). DFT calculation was performed on Australian Synchrotron Compute Infrastructure (ASCI). The MD simulation was undertaken with the assistance of resources and services (the National Key Research and Development Program of China, ISTCP, 2016YFE0101200) from Soochow University. All data are reported in the main text and the Supplementary Materials. **Funding:** This work was supported by Australian Research Council Research Hub for Energy-Efficient Separation (IH170100009). M.J. thanks Monash University and the Monash Centre for Atomically Thin Materials (MCATM) for the scholarships. **Author contributions:** X.Z. and M.J. designed the project. M.J. carried out the experiments and analysis with help from Y.X. and J.L. R.Q. carried out MD simulations and data analysis. Y.C. helped in TEM characterizations. Q.G. contributed to synchrotron characterization and DFT calculations. R.L., C.H., J.Q., and H.W. participated in discussions and analyzed the data. M.J. and X.Z. wrote the manuscript with input from all authors. **Competing interests:** M.J. and X.Z. are inventors on a patent application related to this work filed by Monash University (Australian Provisional Patent Application No. 2020900819, filed 17 March 2020). The authors declare that they have no other competing interests. **Data and materials availability:** All data needed to evaluate the conclusions in the paper are present in the paper and/or the Supplementary Materials. Additional data related to this paper may be requested from the authors.

Submitted 14 June 2019
Accepted 1 April 2020
Published 5 June 2020
10.1126/sciadv.aay3998

Citation: M. Jian, R. Qiu, Y. Xia, J. Lu, Y. Chen, Q. Gu, R. Liu, C. Hu, J. Qu, H. Wang, X. Zhang, Ultrathin water-stable metal-organic framework membranes for ion separation. *Sci. Adv.* **6**, eaay3998 (2020).